

Full Length Article

Enhanced mechanical properties and in vitro biocompatibility of TiMOVWCr high-entropy alloy synthesized by magnetron sputtering

Khurshed Alam ^{a,b,1}, Geonwoo Jeong ^{a,1}, Woohyung Jang ^{c,*}, Hoonsung Cho ^{a,*}^a School of Materials Science & Engineering, Chonnam National University, Gwangju 61186, Republic of Korea^b Powder Materials Division, Korea Institute of Materials Science, 51508 Changwon, Republic of Korea^c Department of Prosthodontics, School of Dentistry, Chonnam National University, Gwangju, Republic of Korea

ARTICLE INFO

ABSTRACT

Keywords:

High-entropy alloy thin film
Surface analysis
Atomic size difference
Enthalpy of mixing
Magnetron sputtering
Hardness and modulus

This study proposes the synthesis of a high-entropy alloy (HEA) composed of TiMOVWCr and a new synthesis route specialized for high-entropy alloys (HEAs) using radio-frequency (RF) magnetron sputtering. The development of HEAs with diversification for various elements is paramount for bridging some limitations in the usage of materials in harsh environments. In developing HEA-preparation techniques, the emergence of a novel sputtering target system is promising for preparing a wide range of HEAs. Thus, a reproducible single target sputtering system is proposed for HEAs and is evaluated systematically. This new target-preparation technique aids in tailoring the elemental compositions to optimize the alloy for important mechanical and biomedical applications, e.g., titanium implants. Films are analyzed using X-ray diffraction (XRD), X-ray photoelectron spectroscopy, and field emission scanning electron microscopy cross-sectional thickness. XRD and valence electron concentration (VEC) data showed a body-centered cubic structure with a major peak orientation of (110). Additionally, this alloy exhibited a very high hardness (29.2 GPa (± 1.5)), elastic modulus (321 ± 8.9 GPa), smooth surface, and good cell viability compared to CP-Ti. The remarkably high hardness and elastic modulus are compared with the literature. Further, the crystalline phase is obtained at room temperature (RT) without undergoing post-treatment.

1. Introduction

Since Yeh et al.'s discovery of high-entropy alloys (HEAs) in 2004, researchers have had access to an alloy system with five or more equimolar primary elements [1]. Each element has a similar probability of filling the lattice sites in a crystal structure in HEAs [2]. The core effects distinguishing HEA from conventional alloys (CAs) are cocktail effects, sluggish diffusion, high entropy, and lattice distortion [2]. These core effects have been identified as the primary factors influencing the improvement in properties, including ductility, oxidation/wear resistance, tribocorrosion, erosion, high mechanical properties, and good corrosion resistance [2]. These properties depend upon the varied compositions of various elements and processing route that is used to develop the final product with exceptional properties [3]. Extensive research has been conducted to develop new types of HEA thin films and bulk materials to improve and advance the properties of CAs [3]. Thus, researchers are currently striving to explore a new type of alloy with a

minimum of five elements with a composition range of 5–35 at% for desired applications to surpass the limitations of CAs [2].

HEAs have drawn considerable research interest owing to their applications in a wide temperature range, high strength, excellent corrosion, and wear resistance [3]. The unusually high hardness of HEAs renders high wear resistance, making the alloy highly reliable for protection purposes [4]. These days researchers have defined that the broadly used bio-implants are titanium-based due to their excellent resistance to corrosion, good mechanical properties, and highly biocompatible for dental and orthopedic implants [5]. But still, there is a research gap and a need to develop further HEAs with good strength for highly corrosive environments [6]. HEAs containing a minimum of five elements render composite effects at the final product with superior mechanical and physical properties; thus, HEAs are more appropriate for wear-resistant prostheses for hip, knee, and shoulder joints [6,7].

Therefore, researchers have also explored the potential of HEAs as biomaterials because of the diverse tailoring ability of HEAs with

* Corresponding authors.

E-mail addresses: awj568@jnu.ac.kr (W. Jang), cho.hoonsung@jnu.ac.kr (H. Cho).

¹ Khurshed Alam and Geonwoo Jeong contributed equally to this work.

various compositions and the type of elements; thus, different types of HEAs can be prepared for desired applications [8]. For example, TiZrNbTaFe reported better corrosion resistance and high hardness in comparison to Ti-6Al-4V [9]. The TiZrHfNbTa alloy demonstrates good wear and pitting resistance, along with favorable mechanical properties and a low tendency towards magnetism [10]. This is in contrast to 316L, CoCrMo, and Ti-6Al-4V, making the alloy suitable for use as an implant material [9]. Furthermore, designing the Bio-HEAs, the importance of low elastic modulus in comparison to bones should be considered to avoid stress shielding effects [5,11]. The ultra-high hardness and a higher elastic modulus reported here may not entirely fit the condition required as a bone replacement implant, due to stress shielding effect, and further endeavor is required to be considered for high load-bearing prostheses and, more specifically, a promising candidate for high wear and frictional areas in high technology applications [11].

Some HEAs developed with high strength, wear resistance, and toughness are MoTaWNbV, HfNbTiZr, TaNbHfZrTi, HfMoTaTiZr, HfMoNbTaTiZr, and CuMoTaWV [3,12–15]. It is of the view that the failure of the materials usually instigates due to wear and friction, ultimately leading the material to failure [16]. To enhance the service life of the metallic materials, and limit such failures, the development of alloys with high wear resistance, elastic modulus and hardness are highly demanded [16]. Some of the metals are well known for their excellent behavior in a physiological environment and are considered highly biocompatible. Nevertheless, a few metals cause severe allergic and adverse effects, causing ultimate failure and inflammations, e.g. Ni and Be [7,17–20].

The most widely used biocompatible materials are stainless steel, Co-Cr, and CP-Ti alloys [7]. They are applicable not only for a short period but also result in localized corrosion when exposed for longer periods in a physiological environment [7]. These materials cause the accumulation of metal debris in soft body tissues as a result of abrasion and wear due to high-movement prostheses, causing allergic reactions and various inflammations [7]. Nevertheless, these issues are addressed using a combination of refractory elements in the form of HEAs having good wear resistance, high biocompatibility, and limited leaching of metals ions into the body's soft tissues in comparison to biomaterials made of CAs [7]. After the development of HEAs, researchers were able to design alloys for diverse structures and biomedical applications owing to their high strength, structural stability, and biocompatibility [7]. Because of the unique core properties of HEAs, they are highly suitable as medical implants because they exhibit excellent surface properties in a physiological environment [7,21,22].

A well-known HEA i.e. TiZrNbMoTa prepared by a casting route, has an issue concern that needs to be processed at a very high temperature. For example, the melting point of Nb is over 3000 °C [5]. Some thin films made of HfNbTaTiZr and MoNbTaTiZr have shown good biocompatibility, adhesion, and pre-osteoblast cell (MC3T3-E1) viability [7]. The alloy design for HEAs has accordingly been explored in the last few decades because of its high importance given its diverse exceptional properties [3]. Thus, researchers have initiated an in-depth exploration of the HEAs [3]. Furthermore, the high number of elements in HEAs requires many materials, making its production slow and costly [3]. Therefore, a new synthesis technique is required to enable fast synthesis with tailororable composition and elements of interest for desired applications [3]. Accordingly, making HEAs synthesis fast, minimizing equipment usage, substituting the element with desired properties, and controlling its composition precisely are the main objectives of this research.

In regarding the disadvantages of high-cost route i.e. casting at high temperature, thus we modified the surface of commercially pure titanium (CP-Ti) substrate with a TiMoVWC thin film at room temperature. And to address the aforementioned problem regarding the need for developing HEAs with high hardness and elastic modulus. We synthesized HEA with remarkably high hardness and elastic modulus for a wide range of application. The thin film was prepared by radio-frequency (RF)

magnetron sputtering with a tailorable single-target system. In addition to the combination of elements, this single-target facility can be applied by varying the composition and replacing the element of choice. In addition, it is prepared at RT using thermodynamic parameters, atomic size difference (δ), enthalpy of mixing (ΔH_{mix}), and configurational entropy (ΔS_{mix}). The values for δ , ΔH_{mix} , and ΔS_{mix} come in the range of the solid solution given [23]. The RT synthesis of the crystalline phase is attributed to the high configurational entropy that causes sluggish diffusion. The developed alloy exhibited high wear resistance, good corrosion resistance, and biocompatibility. The alloy showed robust hardness and elastic modulus compared to the high hardness and elastic modulus reported by NbMoTaW, TaNbHfZr, TiTaHfNbZr, HfNbTiVZr, CuMoTaWV, CoCrFeMnNi, Ti-Nb, TiZrNbTaHf, TiNbZr, TiNbZrTa and TiAlFeCoNi HEAs [2,9,24].

2. Materials and methods

2.1. Target preparation and thin-film coating

The target materials with 99.9 % pure elemental pieces were arranged in a single-target system. The target material components were assembled after being polished with emery paper. The single-target sputtering system, element replacement, or tailoring target composition for potential applications are quick and reproducible. The target can be used for a variety of HEA thin films with tailororable composition as shown in Fig. 1 and the table of content target piece assembly. The target is 4" in diameter, with the distance between the target and the substrate provided being 8 cm. The prepared target is then utilized using very common RF sputtering equipment. The RF target placement configuration is above the substrate. The substrate setting is at the bottom and can be loaded and unloaded by using connected load lock chamber. The magnets are geometrically arranged below the target holder with opposite poles to confine the plasma to the center. RF power was 200 W for a deposition period of 30 min with circular rotation of the substrate set at 10 RPM for uniform coatings. Furthermore, the details of the coating process are also given in Table S1. All the coatings were prepared at RT, and no post-heat treatment was provided.

2.2. Physicochemical, structural, morphological, and mechanical characterization

The homogeneity of the deposited thin films was investigated using EDS (Oxford). XPS was performed to compare the surface chemistry and oxidation states before and after argon etching (Model: K-ALPHA +) using an Al K α X-ray analyzer with photon 1486.6 eV and 180° double focusing hemispherical analyzer (EX06 Ion Gun) and the peak fitting is performed using CasaXPS software. XRD measurements (with Cu K radiation) were performed to examine the crystallinity and phase structure at 45 kV. The thickness of the thin films was measured by FE-SEM (Model: Gemini 500). Atomic force microscopy (AFM) analyses for surface morphology were performed using the NX20 atomic force microscope with noncontact mode. A piezo scanner (size: 100 × 100 × 15 μ m) was used for the precise movement. Further, a nanoindenter was employed to measure nanoindentation, and a maximum load of 3 mN was applied (Type: Berkovich Serial number: BBB-39 Material: Diamond). The values for hardness and elastic modulus were computed under loading and unloading circumstances. Corrosion analysis was performed by utilizing a VSP-300 potentiostat/galvanostat (model number KKR-21738740-40000018) with a maximum volume of 250 mL in a KO235 flat cell kit. The results of corrosion were analyzed using EC-Lab V11.33 software. A constant flow of argon gas (1 SCCM) was supplied to maintain ion homogeneity in an aqueous Ringer's physiological solution. A mixture of NaCl (9 g/L), CaCl₂ (0.24 g/L), KCl (0.43 g/L), and NaHCO₃ 0.23 g/L was used as an electrolyte (Ringer's physiological solution).

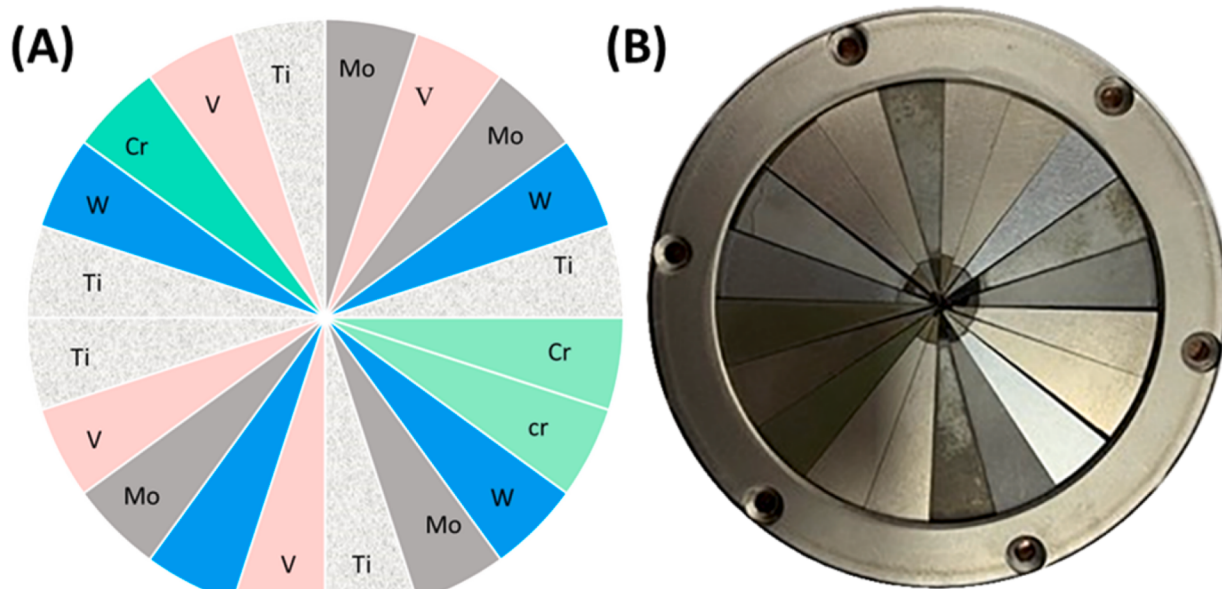


Fig. 1. A) rf/dc magnetron sputtering system for thin-film coating. b) digital photograph of the target.

2.3. Biological characterization

An osteoblast cell line (MC3T3-E1) purchased from ATCC was cultured in alpha MEM media (LM008-53). The media was supplemented with 10 % fetal bovine serum (FBS) and 5 % penicillin-streptomycin. The cultured cells were grown in a T-75 flask in an incubator under 5 % CO₂ environment at 37 °C. Every alternate day, the

media was changed with a fresh one, and the confluent cells in the T-75 flask were sub-cultured for experiments and further passaging.

To assess cell viability (MC3T3-E1), CP-Ti and CP-Ti coated with HEA substrate are used. A cell density of 5×10^4 cells/well was used in 24-well plates in 1-mL alpha MEM media (LM008-53). The cells were allowed to attach at the bottom for three days in a 5% CO₂ atmosphere at 37 °C. After three days of incubation, the media was taken out and

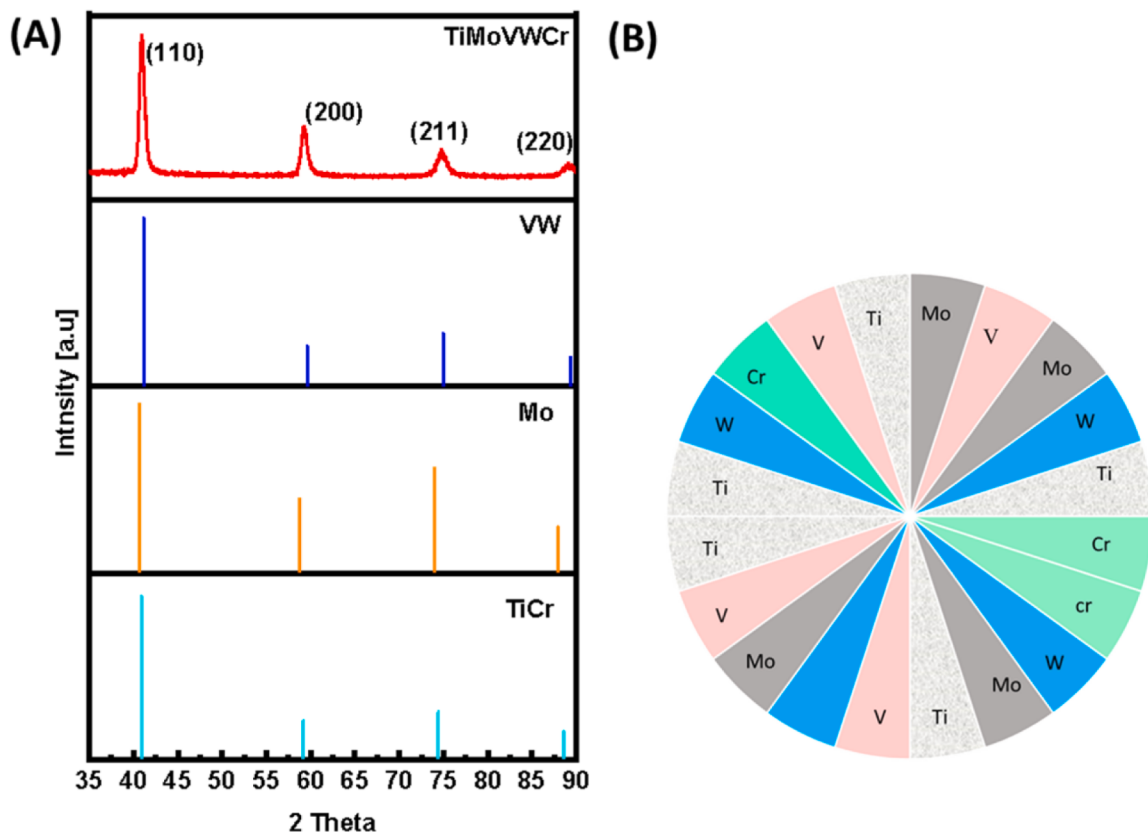


Fig. 2. TiMoVWCr a) XRD peak along with reference data from HighScore Plus and b) configuration of the corresponding target element.

washed twice with 1X phosphate-buffered saline (PBS), followed by 10 % MTT assay ((3-(4, 5-dimethylthiazol2-yl)-2, 5-diphenyltetrazolium bromide). After 2 h, the media was replaced with dimethylsulfoxide (DMSO). The absorbance was measured at 570 nm using a Varioskan lux reader to assess cell viability. Furthermore the cell response and morphology to the surface is studied by Nikon inverted microscope eclipse DS-Ri2, Qi2 (Ex/Em, 405 nm/460 nm; exposure time, 10 s) and the Kit used is cell viability Assay (Fluorometric – Blue Ex 405 nm, ab176748). The cell seeding and incubation remained similar to the cell viability, however 20 μ L of DMSO is added into the vial of CytoCalcein

Violet 450, AM and mixed well. Add the entire contents of CytoCalcein Violet 450, AM stock solution with 10 mL of Assay Buffer, ensuring thorough mixing. The resulting working solution remains stable for at least 2 h when stored at room temperature. After incubating the cells for 3 days, removed the media by suction, and then added 200 μ L of the compound buffer to each well. Allow the cells to be exposed to the compound for 1 h. Next, replace the buffer with fresh media. Finally, transferred the metal sample to a Glass bottom dish (Cellvis, D35-20-1.5-N).

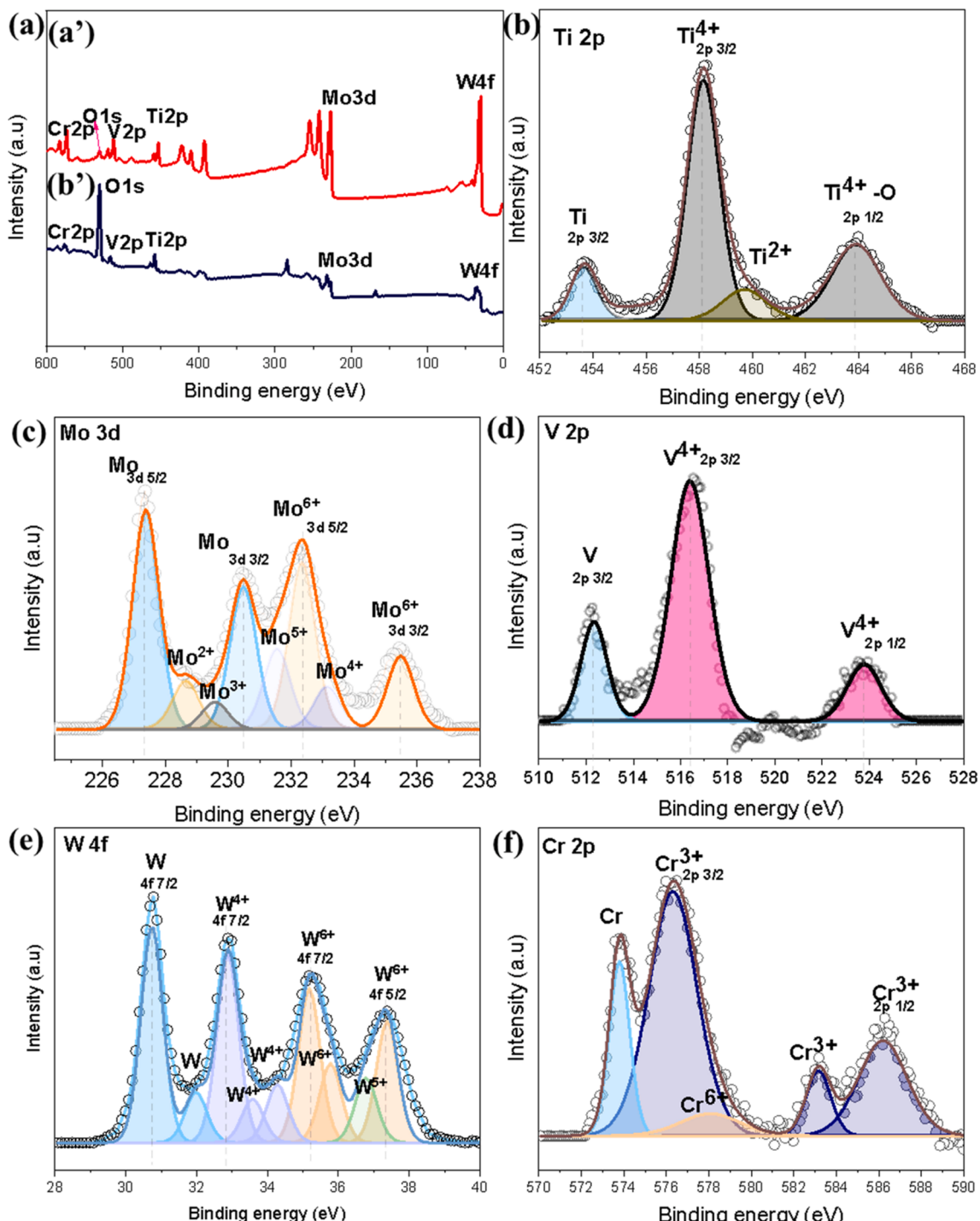


Fig. 3. Chemical bonding state of the TiMoVWWCr HEA thin film analyzed through XPS. a) XPS survey spectra: (a') after Ar⁺ etching and (b') before Ar⁺ etching. b) Ti 2p, c) Mo 3d, d) V 2p, e) W 4f, and f) Cr 2p.

3. Results

3.1. Structural, compositional, and electrochemical analyses

The XRD analysis of TiMoVWCr (HEAs) was performed as shown in Fig. 2 to confirm the formation of the crystalline phase. Various peaks appeared at 410, 590, 74.70, and 890 nm, corresponding to (110), (200), (211), and (220), respectively, in the analysis with X'Pert HighScore Plus, confirming the body-centered cubic (BCC) phase with a major peak orientation of (110). The crystallite size was measured using

the Scherrer equation [25].

$$L = \frac{k\lambda}{\beta \cos\theta}, \quad (1)$$

where L is the grain size, k is the shape factor (0.89), λ is the wavelength ($\text{Cu } k\alpha = 0.154 \text{ nm}$), θ is the diffraction angle, and β is the full width at half maximum obtained from XRD data. The crystallite size thus obtained for the solid solution of TiMoVWCr using the following formula is given in Table S2:

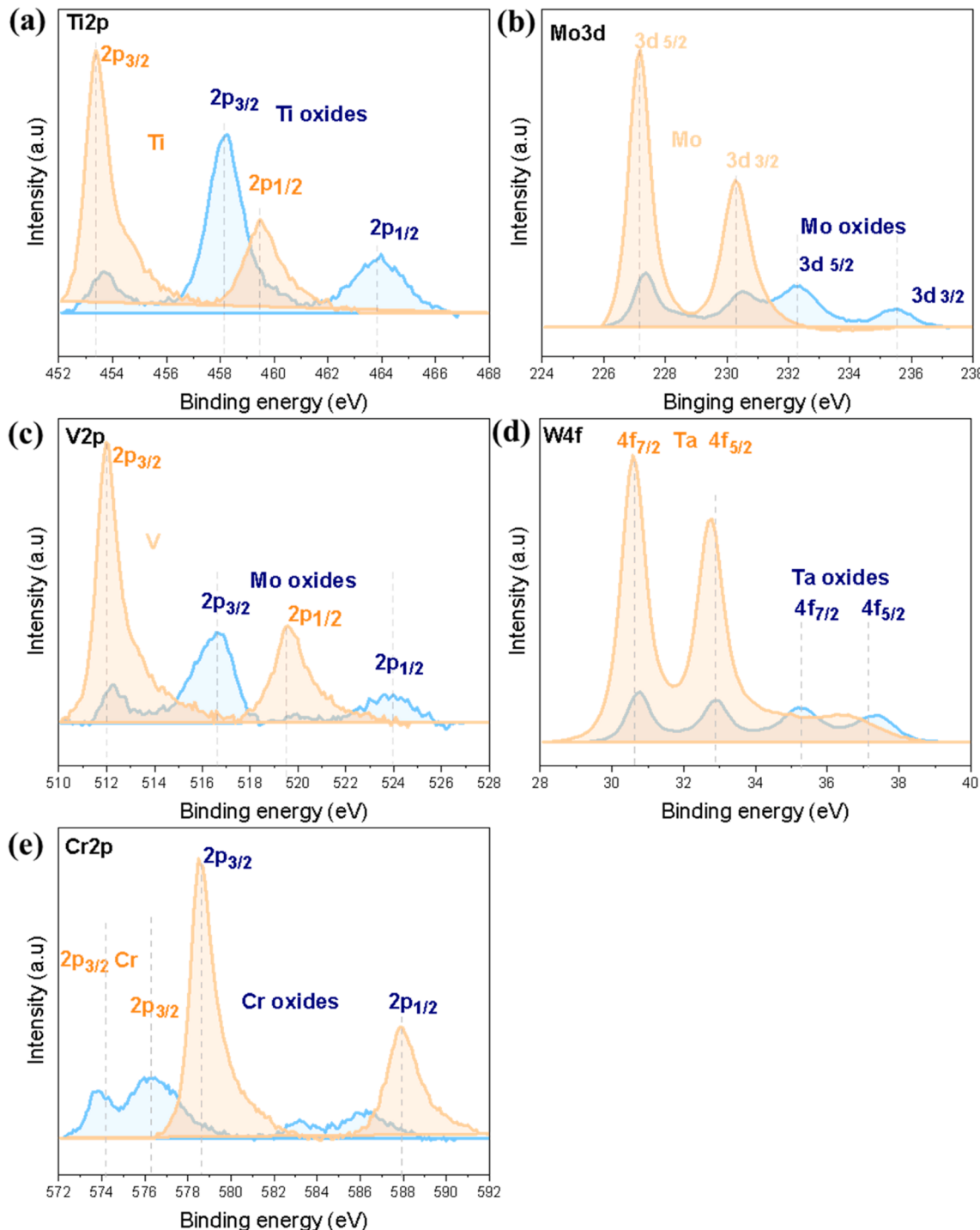


Fig. 4. XPS results showing the oxidation state of the TiMoVWCr HEA after merging the peaks before (blue) and after Ar^+ etching (orange). a) Ti 2p, b) Mo 3d, c) V 2p, d) W 4f, and e) Cr 2p. (For interpretation of the references to colour in this figure legend, the reader is referred to the web version of this article.)

$$a_{mix} = \sum_{i=1}^n c_i a_i. \quad (2)$$

As the CP-Ti surface modified with TiMoVWCr HEA showed better cell viability, detailed XPS was performed to study the surface chemical states of each element individually. Fig. 3a depicts the XPS survey scan showing that all the elements are deposited. Fig. 3a' corresponds to after Ar⁺ plasma etching, showing an increment in individual elements and reduction in the O1s peak. However, the surface before Ar⁺ plasma etching is oxidized, as shown in Fig. 3b', with a high oxygen peak. Fig. 3b shows the fine scan for Ti2p. The major Ti2p3/2 and Ti2p1/2 peaks appeared at 458.2 and 463.9 eV [8]. The peak at 453.6 eV corresponds to a pure metallic state [8]. The peaks at 458.2 and 463.9 eV belong to TiO₂ (4+) [8]. The smaller peak at 459.7 eV may have occurred owing to the oxygen vacancy generated and caused the lower oxidation state for Ti i.e., TiO (Ti²⁺) [26]. Fig. 3c depicts the fine scan deconvoluted for Mo 3d. The major peaks for (Mo⁶⁺) were as follows: Mo3d5/2 at 232.3 eV and Mo3d3/2 at 235.4 eV [27]. The peaks that appeared at 227.3 (Mo3d5/2) and 230.4 eV (Mo3d3/2) are attributed to the pure metallic state (Mo⁰) [27]. Mo3d5/2 peaks at 228.6 and 229.6 eV were attributed to Mo²⁺ and Mo³⁺, respectively [27]. Further, peaks at 231.5 (Mo3d5/2) and 233.1 eV (Mo3d3/2) belong to Mo⁵⁺ and Mo⁴⁺ [27]. Thus, the major peaks belong to the pure metallic state and Mo⁶⁺ (MoO₃) [8,27]. Fig. 3d shows a fine scan for V2p, where V2p3/2 appears at 512.2 eV, belonging to a pure metallic state, i.e., V⁰, and the peak at 516.3 eV belongs to VO₂ (V⁴⁺) [8,28]. Similarly, the V2p1/2 peak appearing at 523.8 eV is also attributed to VO₂ (V⁴⁺) [28]. Fig. 3e illustrates the peak deconvoluted for W4f. The peaks appearing at 30.7, 32.9, 35.2, and 35.7 eV belong to W 4f7/2 and are attributed to pure tungsten (W⁰), WO₂, and WO₃ [29,30]. The W 4f7/2 peaks at 31.9 and 33.5 eV are attributed to the metallic and intermediate state of tungsten (W⁴⁺) [31]. The W 4f5/2 peaks appearing at 37.3 and 34.2 eV are attributed to WO₃ and WO₂, respectively [29]. Similarly, the final peak in Fig. 3f belongs to Cr2p. The peaks for Cr 2p3/2 and Cr 2p1/2 appeared at approximately 576.3 and 586.2 eV with the functional group of Cr₂O₃ [3,32,33]. The peak at 573.8 eV (Cr2p3/2) belongs to the pure metallic state of chromium (Cr⁰) [33,34]. The minor peak obtained at 578.2 eV corresponds to CrO₃ 2p3/2 [33]. Similarly, the peak obtained at 583.1 eV belongs to Cr₂O₃ 2p1/2 (Cr³⁺) [35].

Furthermore, Fig. 4 shows a detailed XPS analysis of before Ar⁺ etching (blue curves) and after Ar⁺ etching. The coated samples were highly susceptible to spontaneous oxidation (3–10 nm) in an open environment [8]. Moreover, as XPS analysis is a specialized tool for surface analysis, surface analysis before Ar⁺ (blue curves) and subsurface analysis after Ar⁺ etching for 20 min (orange curve) to remove

the oxide layer were conducted. The elements shown in Fig. 4 are oxidized (blue curve), and a highly pure metallic state was obtained after Ar⁺ etching (orange curve).

The electrochemical measurements were performed in an aqueous Ringer's physiological solution. The electrolytes used were NaCl (9 g/L), CaCl₂ (0.24 g/L), KCl (0.43 g/L), and NaHCO₃ (0.23 g/L). Fig. 5 a) shows that the corrosion analysis started in a stable condition. In addition, it shows that after letting the samples sufficiently submerge in the solution, a nobler steady state was obtained for HEA than the Ti control. A similar noble behavior was observed in a real-time potentiodynamic experiment. Potentiodynamic curves for the control (Ti) were better passivated spontaneously in a wider passivation region than TiMoVWCr HEA. However, no pitting corrosion was observed, whereas pitting corrosion occurs when the potentiodynamic curve is parallel to the x-axis (current density) [36]. The values obtained through EC-Lab software, namely, I_{corr}, I_{pass}, E_{corr}, and corrosion rate, as presented in Fig. 5 b) are summarized in Table 2. Additionally, the potentiodynamic curves in Fig. 5 b) and Table 3 reveal that TiMoVWCr has lower corrosion density (I_{corr}) than pure titanium, which is the best fit as a corrosion-resistant coating, particularly as an implant because the corrosion media used is similar to the human physiological environment (Ringer's solution). Table 4 is used for finding ΔH_{mix}.

3.2. Microstructural and surface morphology analyses

To determine the cross-sectional film thickness, FE-SEM cross-sectional analysis was performed. The film thickness was measured at various deposition times. The film thickness at 10, 30, 60, and 85 min was 279 nm, 790 nm, 1.2 μm, and 1.9 μm, respectively, as shown in Fig. S1. The corresponding chemical compositions given in Table S3

Table 1
Parameters for designing a solid solution of TiMoVWCr HEA.

Parameters	Literature Values	Experimental Values
ΔS _{mix}	12 ≤ ΔS _{mix} ≥ 17.5 (J/K-mol)	1.6R = 13.3 J/K-mol
ΔH _{mix}	-15 < ΔH _{mix} < 3.2 (kJ/mol)	-3.32
Ω	≥1.1	10.4 (>1)
δ	≤6.6 %	5.98
Valence electron concentration (VEC)	VEC ≥ 8.0 (FCC) VEC ≤ 6.87 (BCC) 6.87 < VEC < 8.0 (BCC + FCC)	5.45 (<6.87) (BCC)

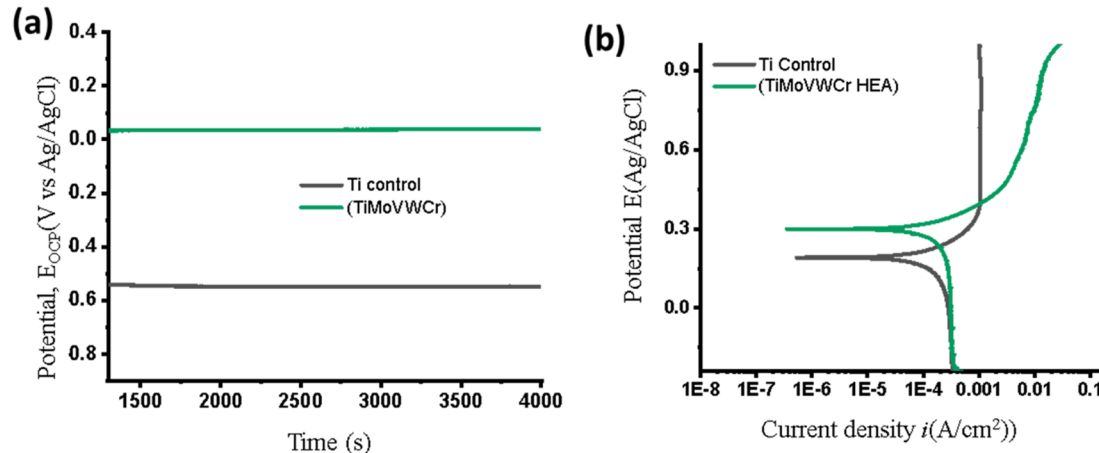


Fig. 5. A) open-circuit potential (e_{ocp}) for the TiMoVWCr HEA and CP-Ti b) potentiodynamic polarization curve of TiMoVWCr HEA and CP-Ti immersed in physiological Ringer's solution at RT prior to potentiodynamic analysis.

Table 2

Corrosion analysis of TiMoVWCr at RT using Ringer's solution.

Samples	E_{corr} (V)	I_{corr} ($\mu A/cm^2$)	β_a (V)	β_c (v)	CR (mmpy)
Ti (Control)	0.19	0.15	0.177	0.612	1.23×10^{-3}
TiMoVWCr (HEA)	0.29	0.11	0.098	0.297	0.07

Table 3Elastic (E) and hardness (H) elastic and plastic deformation (H/E and H^3/E^2 , respectively). The elastic modulus and hardness values were obtained from nanoindentation.

Sample	E (GPa)	H (GPa)	H/E	H^3/E^2 (GPa)
TiMoVWCr (HEA)	321 (± 8.9)	29.2 (± 1.5)	0.09	0.24

Table 4Mixing enthalpy ΔH_{i-j} calculated by Miedema's model for the i-j atomic pair [40].

Ti	Mo	V	W	Cr
Ti	-4	-2	-6	-7
Mo		0	0	0
V		-1	-2	-1
W				1
Cr				

reveal a constant composition range as depicted in Fig. S4a. The constant composition for the HEAs as shown in Fig. S4a and S4c is independent of the deposition time. Nevertheless, the composition can vary if the ratio and elemental configuration of a configurable target change. Fig. S2 presents the EDS layered image showing the nanocolumnar structure, where S2(b-f) correspond to the successful deposition of all the target elements. The corresponding EDS spectrum is shown in Fig. S3. The calculated linear regression (R^2) is 0.93 with a slope of 19.6 and y-intercept $c = 195.3$, as shown in Fig. S4b. The predicted R^2 value is near 1, which indicates a linear relation of the film thickness growth with the time variation. The film was grown with an average deposition rate of 24.5 nm/min. Fig. 6 depicts the cross-sectional image, showing a nanopillar-like morphology, and Fig. 6b shows the composition in different regions of the film at the surface (before Ar^+ etching), sub-surface (after Ar^+ etching) exposing the inner native surface, and bulk, showing a high percentage of oxygen content on the surface. An additional surface morphology study was conducted using AFM. The

surface morphology shown in Fig. 7 has a smooth surface. The root-mean-square roughness $Rq = 0.6 (<1)$ and average roughness $Ra = 0.5 (<1)$, indicating the deposition of a thin film with a highly smooth texture and less porosity. Thus, a highly smooth surface was obtained for TiMoVWCr HEAs.

3.3. Mechanical characterization, MTT cell viability and cell response to the surface coatings

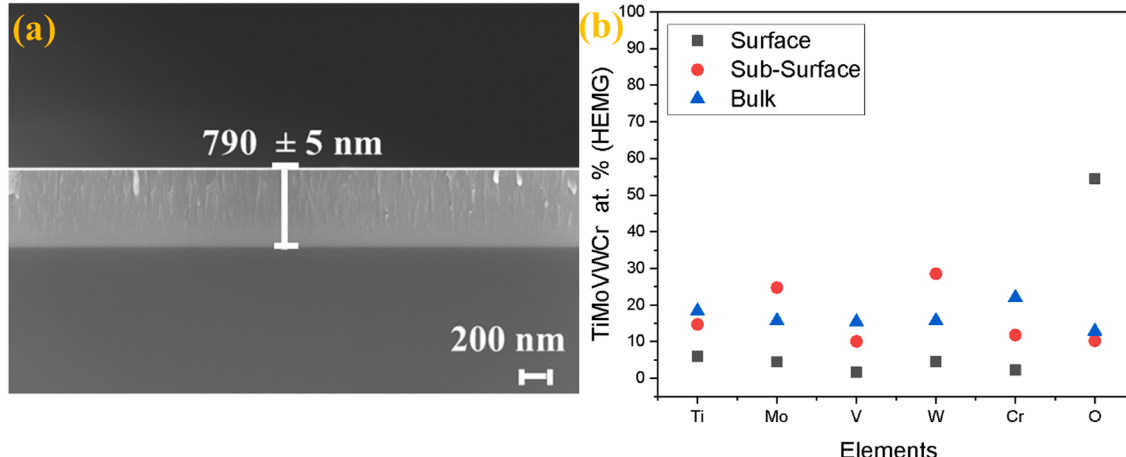
Nanoindentation analysis was conducted with a maximum applied load of 3 mN and a holding time 3 s. The graph for load vs. penetration depth is plotted in Fig. 8. The allowed maximum penetration depth was up to 10% of the coating to avoid the substrate effect [2]. The designed and developed alloy exhibited a high hardness and elastic modulus of 29.2 and 321 GPa, respectively. In addition, this alloy had a higher elastic deformation (H/E) of 0.09 and plastic deformation (H^3/E^2) of 0.24 GPa. The parameters H/E and H^3/E^2 indicate the elastic and plastic flow resistance, respectively [8,37]. Apart from these two mechanical properties, these parameters (H/E and H^3/E^2) indicate wear resistance [8,37]. Thus higher wear resistance is obtained from biocompatible NbTaTiZr HEA showing H/E of 0.052 and H^3/E^2 of 0.017 GPa [8]. This higher hardness is obtained because of the combination of elements with higher hardness and modulus.

Further, a biological test was performed on CP-Ti and its modification with TiMoVWCr HEA using MC3T3-E1 pre-osteoblast cells (purchased from ATCC) for cell viability. Twenty-four-well plates with 1-mL alpha MEM culture media (LM008-53) were used to seed MC3T3 cells at a density of 5×10^4 cells/well. The cells were allowed to attach at the bottom by providing an environment of 37 °C and 5% CO₂ in an incubator. After three days of incubation, the media was removed and washed twice with 1X PBS; then, 0.1-mg/mL MTT (3-(4,5-dimethylthiazol-2-yl)-2,5-diphenyltetrazolium bromide) was used with 10 % in each well. After 2 h in the incubator, the media was replaced with DMSO. To measure cell viability, absorbance measurements were made at 570 nm using a Varioskan lux reader.

The high cell viability and for TiMoVWCr HEA compared to CP-Ti was due to the highly stable passive layer [6]. This layer protects the alloy surface from surrounding simulated body fluids (SBF) [6]. The oxide layer made of Ti, Mo, V, W, and Cr is highly stable and prevents the release of toxic ions [38,39].

4. Discussion

A single-target system was used to reduce preparation time and optimize costs, as illustrated in the table of contents. The target combination of TiMoVWCr was chosen to synthesize HEAs with high

**Fig. 6.** (a) FE-SEM cross-sectional analysis of the TiMoVWCr thin film. (b) Compositional comparison at the surface (XPS), sub-surface (XPS), and in bulk (SEM-EDS).

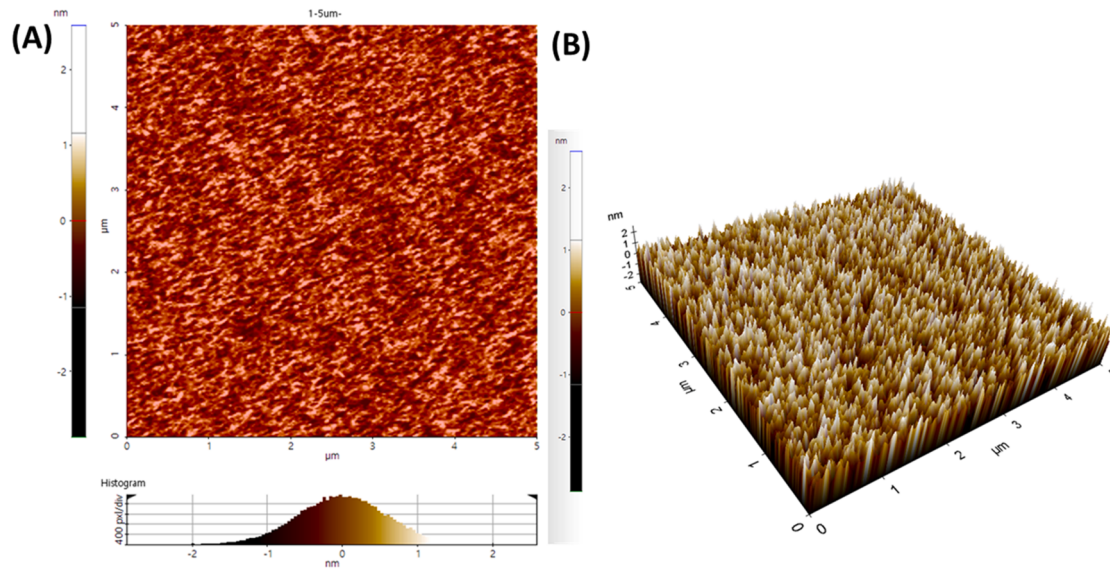


Fig. 7. Surface morphology study of TiMoVWCr by AFM.

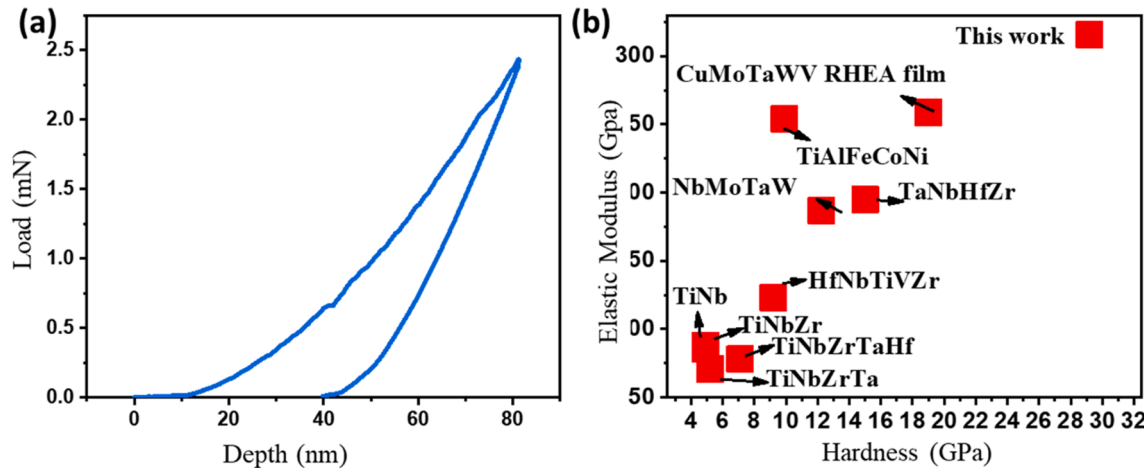


Fig. 8. Nanoindentation plot with a 10% depth (80 nm) of load against penetration depth: a) TiMoVWCr and b) comparison of this work with the highest hardness and elastic modulus reported thus far [2,9,24].

hardness and elastic modulus. Ti with a low elastic modulus was intentionally added to compromise the strength and balance hardness, rendering some ductility. Compared to films of HEAs reported in the literature, the newly developed HEA composed of TiMoVWCr demonstrated the highest hardness and modulus, measuring 29.2 and 331 GPa, respectively. Accordingly, the concept of configurational entropy (ΔS_{mix}) was applied, and the crystalline phase was achieved at RT, optimizing the procedure by avoiding further heat treatment. In MTT assay analysis, the TiMoVWCr HEA showed better cell viability compared to CP-Ti. This observation is attributable to the crystalline HEA and diverse physicochemical state of thin-film coatings, and the good biological response is highlighted in these findings.

The synthesis of a solid solution phase for HEAs has been studied and reported in various articles. Various thermodynamic parameters, e.g., δ , electronegativity, valence electron concentration (VEC), ΔS_{mix} , and ΔH_{mix} , have been statistically evaluated for the synthesis of SSs or amorphous phase in HEAs [1,23]. The debate in HEA synthesis is whether a fixed elemental combination will afford a solid solution or an amorphous phase. Or, is the solid solution or amorphous phase predictable in HEA at RT? The answer is yes, if a proper elemental combination with thermodynamic parameters, namely, δ , ΔH_{mix} , Ω , and

ΔS_{mix} , come in the solid solution range as given in Table 1 [1], is used. Thus, before conducting experiments, the main parameter, particularly the atomic size difference (δ)—the primary parameters for crystalline phase descriptor—is calculated using the following equations and appears in the solid solution range, i.e., 5.98, which is ≤ 6.6 [6]. The enthalpy of mixing ΔH_{mix} and Ω parameters are also calculated and lie within the range, i.e., $-3.3, -22 \leq \Delta H_{\text{mix}} \leq 3.2 \text{ kJ/mol}$, and $10.4 (>1)$ using Equations. (4) and (7), respectively [41]. Thus, the validation criteria for δ , ΔH_{mix} , and Ω parameters are validated in the solid solution range given in Table 1 [6]. Furthermore, phase prediction can be achieved by VEC. Each phase has a specified range of VEC, i.e., the FCC and BCC phases coexist at $6.87 \leq \text{VEC} < 8.0$ [42,43]. The BCC phase is stable at $\text{VEC} < 6.8$, whereas the FCC single phase is stable if $\text{VEC} \geq 8.0$ [42–44]. The thin film prepared had a single BCC structure, which was confirmed by both XRD and VEC (5.4 [<6.8]). The target used in this work is reproducible and could comprise a maximum of up to 20 pieces, which can be used as an advantage for tailoring the composition. The purity of each ingredient is always 99.9%. Our findings suggest that the synthesis of HEA solid solution at RT is more probable in an RF sputtering process. A proper combination of target elements can help avoid further heat treatment as observed in this work, where a crystalline

structure was achieved without heat treatment. Thus, the cost for developing highly crystalline implant materials for potential applications could be optimized. The various formulas used in designing HEAs are given below:

$$\delta = \sqrt{100 \sum_{i=1}^r C_i (1 - r_i)^2}, \quad (3)$$

$$\text{where } \bar{r} = \sum_{i=1}^n C_i r_i$$

$$\Delta H_{\text{mix}} = \sum_{i=1, i \neq j}^n (4 \Delta H_{\text{mix}} AB), \quad (4)$$

$$VEC = \sum_{i=1}^N C_i (VEC)_i, \quad (5)$$

$$\Delta S_{\text{mix}} = -R \sum_{i=1}^N C_i \ln c_i, \quad (6)$$

$$\Omega = \frac{T_m \Delta S_{\text{mix}}}{\Delta H_{\text{mix}}}, \quad (7)$$

$$T_m = \sum_{i=1}^N C_i (Tm)_i$$

The synthesis of TiMoVWCr HEA via RF sputtering also affects the composition and crystal structure of the thin-film coating. Therefore, the surface and sub-surface chemical states were studied in detail, as shown in Fig. 3. The compositions for bulk, surface, and sub-surface exhibited all the target elements, i.e., Ti:Mo:V:W:Cr, but with varied compositions for similar coatings as shown in Fig. 6b. This condition proved useful because for biological application surfaces with diverse implant exposed areas, the surface molecular interactions are highly related with the cell response for good cell proliferation [8]. The concentration of V was intentionally reduced, as revealed by Table S3, because most alloys containing V have been reported to show toxicity [8]. An alloy with high V concentration shows various side effects such as immunotoxicity, neurotoxicity, and carcinogenicity [8]. Moreover, as shown by Fig. 6, the surface analyses revealed a highly oxidized surface due to natural passivation. This phenomenon fills the vacancies by oxygen affinity toward the oxidation of metals, promoting the formation of highly stable oxide layers [8]. Thus, with highly oxide-generated surfaces and an alloy with low V concentration, the TiMoVWCr HEA thin-film coatings showed superior cell viability. The results were evaluated by MTT assay at 570-nm absorbance. The stable oxide layers associated with TiMoVWCr HEA are TiO_2 , MoO_3 , VO_2 , WO_2 , WO_3 , CrO_3 , and Cr_2O_3 , favoring the generation of stable and homogeneous protective oxide layers. A similar observation was reported in an article on an NbTaTiVZr-based HEA [8]. However, the authors obtained the crystalline phase after an additional heat treatment [8].

The mechanical properties of the HEA resulted in remarkably high hardness and modulus. Furthermore, it also showed higher elastic and plastic deformation as well as high wear resistance. The elastic (H/E) and plastic (H3/E2) deformation obtained is 0.09 and 0.24 GPa which is much higher than NbTaTiVZr HEA. The H/E and H3/E2 values obtained for NbTaTiVZr HEA are 0.05 and 0.017 respectively [8]. Therefore, this alloy with high hardness, modulus, and wear resistance is also applicable in high-wear and high-strength areas. In particular, when implant materials are implanted in a physiological environment, their service life is limited owing to the combined wear and corrosion environment. Thus, the implant material surface needs to be modified with highly wear-resistant coating [45]. Some Ti-based alloys cause inflammations because of the debris formed by high-wear phenomena in physiological conditions [45]. Hence, an HEA with high wear resistance is crucial for long service life [45]. Additionally, research on cell proliferation and

cells morphology by directly growing cells on the surface was studied. The in vitro evaluation of TiMoVWCr HEA revealed high cell viability as shown in Fig. 9. The cells morphology is studied using florecence microscopy for control, without coating and HEA coatings surfaces. The cells growth response to the surface is studied by assay kit (Fluorometric – Blue Ex 405 nm, ab176748). The cells morphology in Fig. 10 shows healthy growth, however the cells grown on HEA surface has extended shape and it appears that the cells possess extensive cytoplasmic extensions that create a network connecting them to neighboring cells [46]. This high cell viability and MC3T3-E1 cells morphology studied by fluorescence microscopy for HEA can be attributed to the highly smooth surface morphology, which was analyzed by AFM ($R_q < 1$), and nanopillar-like structures as shown in Fig. 7. The surface modification with the nanoscale surface has a positive influence while interacting with cells in terms of proliferation, adhesion of MC3T3-E1 cells, and transducing the signals at the molecular level as biological applications [8].

5. Conclusion

This research proposed and developed a new manufacturing route for HEAs using a single configurable target specialized for HEAs. The proposed system is fast, repeatable, and offers high degrees of freedom for the synthesis of a wide range of HEAs, i.e., the desired elemental range can be varied. The HEA made of TiMoVWCr showed the high hardness and elastic modulus of 29.2 and 331 GPa, respectively. More surprisingly, the crystalline phase was obtained at RT using the concept of high mixing entropy, which allow the phase to grow in the crystalline phase owing to its sluggish diffusion. The calculated thermodynamic parameters, i.e., δ , ΔH_{mix} , and Ω , were used as necessary criteria to form a solid solution. Thus, on the basis of these thermodynamic parameters, the target elements were chosen. The crystallinity was measured by XRD analysis. In addition, the film coating thickness, uniform compositional analysis, and cross-sectional thickness were measured using FE-SEM and EDS analyses. Furthermore, the TiMoVWCr HEA showed better cell viability in the MTT assay analysis. Overall, this study contributes to advancing the surface biocompatibility of coatings on implant materials and also coating materials requiring high wear resistance, hardness, and modulus. The future study on this alloy (TiMoVWCr) will be directed toward controlling the hardness of the thin film by tailoring the surface composition and the MC3T3 pre-osteoblast cell differentiation. Furthermore, additional research is necessary to investigate the potential applications of this alloy, particularly in situations that demand high levels of strength.

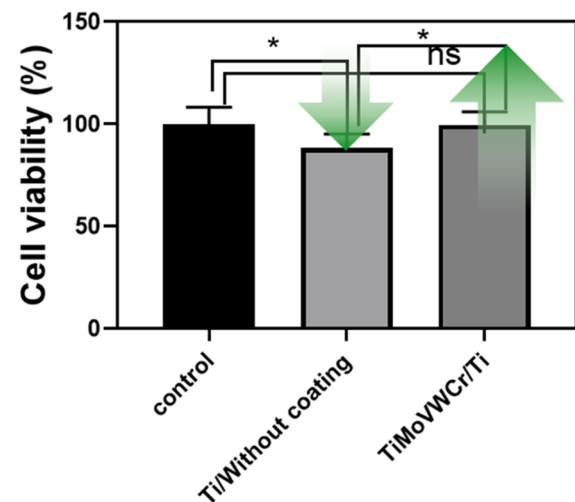


Fig. 9. MTT assay analysis for cell viability after growing MC3T3 cells on various substrates.

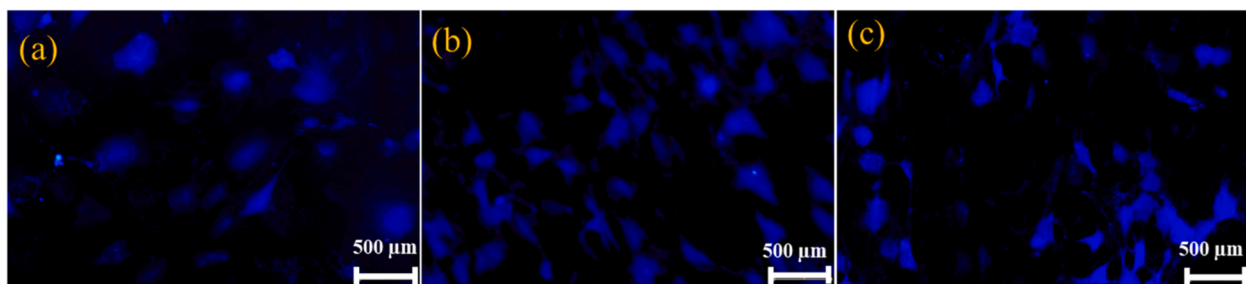


Fig. 10. MC3T3-E1 pre-osteoblast cells biological response, studied by inverted microscope a) cells grown on glass bottom dish (control) (b) cells morphology on Ti substrate (without coating) (c) cells morphology on TiMoVWCr HEA coating.

Declaration of Competing Interest

The authors declare that they have no known competing financial interests or personal relationships that could have appeared to influence the work reported in this paper.

Data availability

Data will be made available on request.

Acknowledgements

This research was supported by Basic Science Research Program through the National Research Foundation of Korea (NRF) funded by the Ministry of Education (No. 2021R1I1A1A01058691) and by a National Research Foundation of Korea (NRF) grant funded by the Korea Government (MSIT) (No. 2021R1F1A1064062).

Appendix A. Supplementary material

Supplementary data to this article can be found online at <https://doi.org/10.1016/j.apsusc.2023.158222>.

References

- [1] S. Guo, C.T. Liu, Phase stability in high entropy alloys: Formation of solid-solution phase or amorphous phase, *Prog. Nat. Sci.: Mater. Int.* 21 (6) (2011) 433–446.
- [2] S. Alvi, et al., Synthesis and mechanical characterization of a CuMoTaWV high-entropy film by magnetron sputtering, *ACS Appl. Mater. Interfaces* 12 (18) (2020) 21070–21079.
- [3] J.X. Yang, et al., Rapid fabrication of high-entropy ceramic nanomaterials for catalytic reactions, *ACS Nano* 15 (7) (2021) 12324–12333.
- [4] X. Hao, et al., Microstructure and wear resistance of in-situ TiN/(Nb, Ti)5Si3 reinforced MoNbTaWTi-based refractory high entropy alloy composite coatings by laser cladding, *Appl. Surf. Sci.* 626 (2023), 157240.
- [5] Y.H. Chen, et al., On the bio-corrosion and biocompatibility of TiTaNb medium entropy alloy films, *Appl. Surf. Sci.* 508 (2020), 145307.
- [6] H. Song, S. Lee, K. Lee, Thermodynamic parameters, microstructure, and electrochemical properties of equiatomic TiMoVWCr and TiMoVNbZr high-entropy alloys prepared by vacuum arc remelting, *Int. J. Refract. Metal Hard Mater.* 99 (2021), 105595.
- [7] J. Shittu, et al., Biocompatible high entropy alloys with excellent degradation resistance in a simulated physiological environment, *ACS Applied Bio Materials* 3 (12) (2020) 8890–8900.
- [8] F. Cemin, et al., Superior in vitro biocompatibility in NbTaTiVZr (O) high-entropy metallic glass coatings for biomedical applications, *Appl. Surf. Sci.* (2022), 153615.
- [9] P. Edalati, et al., Ultrahigh hardness and biocompatibility of high-entropy alloy TiAlFeCoNi processed by high-pressure torsion, *Mater. Sci. Eng. C* 112 (2020), 110908.
- [10] J. Feng, et al., Preparation of TiNbTaZrMo high-entropy alloy with tunable Young's modulus by selective laser melting, *J. Manuf. Process.* 85 (2023) 160–165.
- [11] A. Brizuela, et al., Influence of the elastic modulus on the osseointegration of dental implants, *Materials* 12 (6) (2019) 980.
- [12] O.N. Senkov, et al., Mechanical properties of Nb25Mo25Ta25W25 and V20Nb20Mo20Ta20W20 refractory high entropy alloys, *Intermetallics* 19 (5) (2011) 698–706.
- [13] O. Senkov, et al., Microstructure and elevated temperature properties of a refractory TaNbHfZrTi alloy, *J. Mater. Sci.* 47 (2012) 4062–4074.
- [14] H. Yao, et al., NbTaV-(Ti, W) refractory high-entropy alloys: Experiments and modeling, *Mater. Sci. Eng. A* 674 (2016) 203–211.
- [15] V. Soni, et al., Microstructural design for improving ductility of an initially brittle refractory high entropy alloy, *Sci. Rep.* 8 (1) (2018) 8816.
- [16] C. Feng, et al., High Hardness and Wear Resistance in AlCrFeNiV High-Entropy Alloy Induced by Dual-Phase Body-Centered Cubic Coupling Effects, *Materials*, 2022, 15, DOI: 10.3390/ma15196896.
- [17] B.D. Ratner, et al., *Biomaterials science: an introduction to materials in medicine*, California, San Diego, 2004, pp. 162–164.
- [18] V.K. Balla, et al., Tantalum—a bioactive metal for implants, *JOM* 62 (7) (2010) 61–64.
- [19] R. Tsaryk, et al., The role of oxidative stress in pro-inflammatory activation of human endothelial cells on Ti6Al4V alloy, *Biomaterials* 34 (33) (2013) 8075–8085.
- [20] S. Hadibek, et al., High-entropy alloy-induced metallic glass transformation: challenges posed by *in situ* alloying via additive manufacturing, *Adv. Eng. Mater.* 25 (7) (2023) 2200764.
- [21] O. Senkov, et al., Refractory high-entropy alloys, *Intermetallics* 18 (9) (2010) 1758–1765.
- [22] M. Todai, et al., Novel TiNbTaZrMo high-entropy alloys for metallic biomaterials, *Scr. Mater.* 129 (2017) 65–68.
- [23] S. Guo, et al., More than entropy in high-entropy alloys: forming solid solutions or amorphous phase, *Intermetallics* 41 (2013) 96–103.
- [24] J. González-Masis, et al., Synthesis of biocompatible high-entropy alloy TiNbZrTaHf by high-pressure torsion, *Mater. Sci. Eng. A* 825 (2021), 141869.
- [25] M.A. Ashraf, et al., Effects of annealing treatment on corrosion resistance of arc sprayed aluminum coating, *J. Therm. Spray Technol.* 31 (6) (2022) 1934–1943.
- [26] H. Tan, et al., A facile and versatile method for preparation of colored TiO₂ with enhanced solar-driven photocatalytic activity, *Nanoscale* 6 (17) (2014) 10216–10223.
- [27] C. Castillo, et al., Molybdenum trioxide thin films doped with gold nanoparticles grown by a sequential methodology: photochemical metal-organic deposition (PMOD) and DC-magnetron sputtering, *J. Chil. Chem. Soc.* 61 (2016) 2816–2820.
- [28] M.C. Biesinger, et al., Resolving surface chemical states in XPS analysis of first row transition metals, oxides and hydroxides: Sc, Ti, V, Cu and Zn, *Appl. Surface Sci.* 257 (3) (2010) 887–898.
- [29] L. Carpen, et al., Hybrid nanostructures obtained by transport and condensation of tungsten oxide vapours onto CNW templates, *Nanomaterials* 11 (2021) 835.
- [30] X. Zhang, et al., Pseudocubic phase tungsten oxide as a photocatalyst for hydrogen evolution reaction, *ACS Appl. Energy Mater.* 2 (12) (2019) 8792–8800.
- [31] A.V. Akopyan, et al., New type of catalyst for efficient aerobic oxidative desulfurization based on tungsten carbide synthesized by the microwave method, *ACS Omega* 7 (14) (2022) 11788–11798.
- [32] W. Huang, et al., Epitaxial patterned Bi 2 FeCrO 6 nanoisland arrays with room temperature multiferroic properties, *Nanoscale Adv.* 1 (6) (2019) 2139–2145.
- [33] L. Liao, et al., Novel rotary chemical mechanical polishing on an integral impeller, *J. Manuf. Process.* 66 (2021) 198–210.
- [34] V.B. Pinho, P., et al., Crystal field effects on the photoemission spectra in Cr2O3 thin films: From multiplet splitting features to the local structure, *Materialia* 12 (2020), 100753.
- [35] S.G. Musa, et al., Application of POMOF composites for CO₂ fixation into cyclic carbonates, *IOP Conf. Series Earth Environ. Sci.* 842 (2021), 012046.
- [36] S. Pang, et al., New Ti-based Ti–Cu–Zr–Fe–Sn–Si–Ag bulk metallic glass for biomedical applications, *J. Alloy. Compd.* 625 (2015) 323–327.
- [37] A. Leyland, A. Matthews, On the significance of the H/E ratio in wear control: a nanocomposite coating approach to optimised tribological behaviour, *Wear* 246 (1) (2000) 1–11.
- [38] W. Yang, et al., Bio-corrosion behavior and in vitro biocompatibility of equimolar TiZrHfNbTa high-entropy alloy, *Intermetallics* 124 (2020), 106845.
- [39] S.-P. Wang, J. Xu, TiZrNbTaMo high-entropy alloy designed for orthopedic implants: As-cast microstructure and mechanical properties, *Mater. Sci. Eng. C* 73 (2017) 80–89.
- [40] A. Takeuchi, A. Inoue, Classification of bulk metallic glasses by atomic size difference, heat of mixing and period of constituent elements and its application to characterization of the main alloying element, *Mater. Trans.* 46 (12) (2005) 2817–2829.
- [41] Y. Ye, et al., High-entropy alloy: challenges and prospects, *Mater. Today* 19 (6) (2016) 349–362.
- [42] S. Guo, et al., Effect of valence electron concentration on stability of fcc or bcc phase in high entropy alloys, *J. Appl. Phys.* 109 (10) (2011), 103505.

- [43] X. Chang, et al., Phase engineering of high-entropy alloys, *Adv. Mater.* 32 (14) (2020) 1907226.
- [44] H. Kim, et al., Mechanical and electrical properties of NbMoTaW refractory high-entropy alloy thin films, *Int. J. Refract Metal Hard Mater.* 80 (2019) 286–291.
- [45] J. Feng, et al., Bio-high entropy alloys: progress, challenges, and opportunities, *Metallic Alloys Med. Appl.* (2022) 131.
- [46] M. Pole, et al., Biocompatible high entropy alloys with excellent degradation resistance in a simulated physiological environment, 2021.